J. Fluid Mech. (1998), *vol.* 370, *pp.* 321–345. Printed in the United Kingdom

Unsteady blood flow in a helically symmetric pipe

By L. ZABIELSKI AND A. J. MESTEL
Mathematics Department, Imperial College, 180 Queen's Gate, London SW7 2BZ, UK

(Received 13 March 1997 and in revised form 27 October 1997)

Fully developed flow in a helical pipe is investigated with a view to modelling blood flow around the commonly non-planar bends in the arterial system. Medical research suggests that the formation of atherosclerotic lesions is strongly correlated with regions of low wall shear and it has been suggested that the observed non-planar geometry may result in a more uniform shear distribution. Helical flows driven by an oscillating pressure gradient are studied analytically and numerically. In the high-frequency limit an expression is derived for the second-order steady flow driven by streaming from the Stokes layers. Finite difference methods are used to calculate flows driven by sinusoidal or physiological pressure gradients in various geometries. Possible advantages of the observed helical rather than planar arterial bends are discussed in terms of wall shear distribution and the inhibition of boundary layer separation.

1. Introduction

Many physical processes involve flows driven down curved pipes and a review of this much studied problem is given by Berger, Talbot & Yao (1983). Applications to chemical engineering are manifest, but in this paper particular attention will be given to haemodynamic flows. An essential introduction to the subject can be found in Pedley (1980) and a recent survey in Pedley (1995).

Most theoretical studies on this problem have considered a planar or two-dimensional bend, so that the pipe can be considered as a portion of a torus. If the curvature of such a pipe is small, the problem for steady flows reduces to the Dean (1928) equations. However, in the body the driving pressure gradient is pulsatile, and steady solutions can, at best, be regarded as approximations for conditions at some distance from the heart. Flows around a planar bend assuming a time-sinusoidal pressure gradient have been considered by Lyne (1970), Blennerhassett (1976) and Smith (1975). Lyne calculated the steady flow driven by second-order steady streaming for purely oscillatory flows, and these results are extended in § 3 of this paper. Blennerhassett considered the interaction of such an induced steady flow with a weak mean component of the pressure gradient, finding multiple solutions in some parameter ranges. Smith categorized the possible asymptotic regimes as the parameters vary.

Interestingly, in the body there are several instances where arterial bends occur in a markedly non-planar manner, even when there is no obvious logistical reason why this should happen (Caro *et al.* 1996). The largest such bend is the aortic arch and a recent review of the complex aortic dynamics can be found in Chandran (1993). As the arterial system is old in evolutionary terms it is regarded by physiologists as being

of optimal design, and hence some advantage should accrue from the non-planar bending. One possible advantage would be a degree of equalization of wall shear stress (Caro, Fitz-Gerald & Schroter 1971). It is generally recognized that the wall shear plays an important role in influencing the behaviour of the endothelial cells in the arterial wall. There is evidence that the arterial cross-section adapts so as to reduce excessive shear rates (Kamiya & Togawa 1980) and a general review of the morphology, metabolism and mechanical properties of arterial walls is given by Davies (1995). Inappropriate shear levels may result in disease. High shear stresses may damage the red cells and proteins in the bloodstream, while regions of low wall shear are sites for the build-up of fatty residues and possible atherosclerosis (Schettler *et al.* 1983; Yoshida *et al.* 1988; Giddens, Zarins & Glagov 1993).

As well as aiding fundamental understanding of a healthy body and certain natural diseases, an appreciation of geometrical effects is important in various surgical procedures. When arteries are grafted together, an inappropriate junction geometry can result in the build-up of plaque in low-shear regions leading to a state known as neo-intimal hyperplasia (Dobrin, Litooy & Endean 1989). The condition is less likely to occur if the grafts can be designed to inhibit separation and to equalize the wall shear distribution.

This paper aims to examine the interaction between time-periodic flows and three-dimensional bends. As described in the contiguous paper (Zabielski & Mestel 1998) on steady flows, henceforth referred to as ZM1, the non-planar bend will be modelled by a helical pipe of infinite extent. The curvature and torsion of the helix can be chosen to match various portions of the body. For steady flows, it was not clear that entrance effects could be neglected, but for the rapidly oscillating pulsatile flows in the body, it is arguable that a shorter entrance length will be required for a fully developed flow to be set-up if the arterial transit time is several heart-beats long.

The walls will be assumed to be fixed in space, unlike arteries on the heart surface which necessarily move with the heart-beat (Lynch, Waters & Pedley 1996). Two kinds of pressure pulses will be considered. The first will be sinusoidal with or without a constant mean, whereas the other will use the data of McDonald (1974) to model the physiological pulse. The layout of the paper is as follows:

In § 2, the problem is formulated, summarizing where appropriate the results of ZM1. In § 3, the contribution to the steady flow from the nonlinear interactions of oscillating terms is analysed in the manner of Lyne (1970). It is shown that the effect of the Stokes boundary layers can be represented as an appropriate slip velocity for the core flow. It is argued that torsion will have limited effect on the steady component of the cross-sectional flow, a fact verified in the numerical results of § 4. However, there exists a down-pipe component which for some pipe shapes can carry a net flux even in the absence of a mean pressure gradient. It is also shown numerically that Lyne's vortices, of opposite sense to those of classical Dean (1928) flow, manifest themselves mainly in the small curvature limit. If curvature terms are included explicitly, rather than using the Dean equations, these vortices are notably less pronounced.

As the amplitude of the pulse is increased into the physiologically most relevant range, nonlinear terms become dominant and a richer structure develops. At intermediate values a symmetry-breaking bifurcation is identified, but for higher amplitudes a symmetric solution seems once more to be preferred.

For physiological pulses an interesting effect was found, which may indicate one advantage of non-planar bends. For axisymmetric toroidal pipes, it was found that as the flow reverses in the late systolic part of the cardiac cycle, the boundary layers at the top and bottom of the torus separate off, shedding vortex pairs into the main body

of the fluid. For helical bends however, the shear appeared to remain localized at the inside of the bend. The wall shear is calculated and some degree of equalization of the cross-pipe component is found, although the down-pipe component is relatively unaffected.

2. Formulation of the problem

The motion of an incompressible Newtonian fluid inside a helical pipe is considered. In the fully developed case the flow has helical symmetry with constant pitch ε as defined in ZM1 and also in Childress, Landmann & Strauss (1989), Landman (1990) and Dritschel (1991). This means that the velocity, vorticity and pressure gradient do not vary in the helical direction $\boldsymbol{H}$ which in cylindrical coodinates (r, θ, z) can be expressed as

$$\boldsymbol{H} = \frac{1}{h^2}(-\varepsilon r \boldsymbol{e}_\theta + \boldsymbol{e}_z), \quad \text{where} \quad h^2 = 1 + \varepsilon^2 r^2. \tag{2.1}$$

Hence $\boldsymbol{H}$ is orthogonal to the radial vector $\boldsymbol{e}_r$ and together with

$$\boldsymbol{e}_\phi = h\boldsymbol{H} \times \boldsymbol{e}_r = \frac{1}{h}(\boldsymbol{e}_\theta + \varepsilon r \boldsymbol{e}_z)$$

these form a helical vector base. The vector $\boldsymbol{e}_\phi$ points in the direction of $\phi = \theta + \varepsilon z$. Thus a scalar function f is helically symmetric when $\boldsymbol{H} \cdot \nabla f = 0$, or equivalently $f = f(r, \phi)$.

A helically symmetric, incompressible velocity field can be written

$$\boldsymbol{u} = \boldsymbol{H} \times \nabla \Psi + v\boldsymbol{H}, \tag{2.2}$$

where $\Psi = \Psi(r, \phi)$ is a helical streamfunction and v is the down-pipe velocity component. Similarly, the vorticity $\boldsymbol{\omega} = \nabla \times \boldsymbol{u}$ is given by

$$\boldsymbol{\omega} = \nabla v \times \boldsymbol{H} + \xi \boldsymbol{H} \tag{2.3}$$

which leads to the kinematic relation

$$\mathscr{L}\Psi = \xi + \frac{2\varepsilon}{h^2} v, \quad \text{where} \qquad \mathscr{L} = \frac{h^2}{r}\frac{\partial}{\partial r}\left(\frac{r}{h^2}\frac{\partial}{\partial r}\right) + \frac{h^2}{r^2}\frac{\partial^2}{\partial \phi^2}. \tag{2.4}$$

In the present study, it will be assumed that the flow is driven by an oscillating pressure gradient per unit mass of the form

$$h^2 \boldsymbol{H} \cdot \nabla p = h_b(G + \omega_0 W f(\omega_0 t)). \tag{2.5}$$

Here $h_b = (1 + \varepsilon^2 b^2)^{1/2}$ where b is a typical distance between the pipe and the z-axis (b can be defined with respect to the centre of mass of the cross-section or centreline of the pipe). The constant G represents the steady, mean component of pressure gradient while ω_0 is the frequency and W is a typical oscillation amplitude. The function $f(\omega_0 t)$ is periodic and can always be chosen so that

$$\int_0^T f(\omega_0 t)\mathrm{d}t = 0 \quad \text{and} \quad \frac{2}{T}\int_0^T f(\omega_0 t)\cos(\omega_0 t)\mathrm{d}t = 1 \quad \text{where} \quad T = 2\pi/\omega_0.$$

In the following analysis, cases when $f(t)$ is a simple harmonic $f(\omega_0 t) = \cos(\omega_0 t)$ as well as physiologically relevant shapes of $f(\omega_0 t)$ will be considered.

Using the helical decompositions for the velocity and vorticity fields in (2.2) and

(2.3) and the following scales (a is a typical pipe radius):

$$t \sim \frac{1}{\omega_0}, \quad r \sim a, \quad \frac{\Psi}{a^2}, \ \frac{v}{a}, \ \xi \sim \frac{v}{a^2}\left(\frac{v}{\omega_0 a^2}\right)^{-1/2}, \tag{2.6}$$

the Navier–Stokes equations take the non-dimensional form

$$\frac{\partial v}{\partial t} + \alpha\frac{1}{r}J(\Psi, v) = R\alpha^3 + R_s f(t) + \alpha^2\left(\mathscr{L}v + \frac{2\varepsilon}{h^2}\xi\right) \tag{2.7}$$

and

$$\frac{\partial \xi}{\partial t} + \alpha\left(-\frac{2\varepsilon}{h^2}\frac{1}{r}J(\Psi, v) + \frac{1}{r}J(\Psi, \xi) + \frac{2\varepsilon^2}{h^2}\left(\xi\frac{\partial \Psi}{\partial \phi} + v\frac{\partial v}{\partial \phi}\right)\right) = \alpha^2\left(\mathscr{L}\xi - \frac{2\varepsilon}{h^2}\left(\mathscr{L}v + \frac{2\varepsilon}{h^2}\xi\right)\right) \tag{2.8}$$

where the Jacobian $J(f, g) = \partial(f, g)/\partial(r, \phi)$ and

$$\alpha^2 = \frac{\nu}{\omega_0 a^2}, \quad R_s = h_b\frac{Wa}{\nu}\alpha, \quad R = h_b\frac{Ga^3}{\nu^2}. \tag{2.9}$$

If $f(t)$ is prescribed, equations (2.4), (2.7) and (2.8) together with solid wall boundary conditions determine a general flow with helical symmetry. In addition to the physical parameters of (2.9), the flow depends on the pipe curvature and torsion controlled by a/b and ε respectively.

In (2.9) the parameter α measures the oscillation frequency and $1/\alpha$ is known as the Womersley number. R represents the steady forcing term and can be related to the classical Dean number (D) by $R = D(b/a)^{1/2}h_b$. The parameter R_s measures the amplitude of the oscillating part of the pressure gradient and $(R_s/h_b)^2 a/b$ corresponds to the steady streaming Reynolds number defined by Lyne (1970). Since a helical flow is controlled by so many parameters there exists a great variety of different limiting cases for which an asymptotic solution can be sought. Smith (1975) provides quite an extensive survey on the various possible limits for the axisymmetric problem with small curvature ($b, \varepsilon \to \infty$). The present analysis is intended to concentrate on a case of some physiological relevance and as $\alpha \simeq 0.05$ in the human aortic arch, the limit $\alpha \to 0$ is most appropriate. In the smaller vessels α is larger and the limits $R_s, R \to \infty$ are also of physiological interest (Pedley 1980).

3. Asymptotic analysis of rapidly oscillating flow

It is well known that a rapidly oscillating flow exhibits at leading order a potential core and Stokes-layer structure. The wall shear is found to be proportional to the tangential slip velocity of the inner expansion, for all boundary shapes. However, the second- and higher-order perturbations include nonlinear terms and hence require more particular treatment. Then any symmetry assumptions or choice of coordinates can be crucial in simplifying the problem.

The axisymmetric case ($\varepsilon \to \infty$) has already been studied (Lyne 1970; Blennerhassett 1976; and Smith 1975). The present work aims to extend some of those results to the helical case and to investigate the geometrical effects due to non-zero torsion and $O(1)$ curvature. In almost all former studies the curvature has been assumed to be small so that the Dean equations of motion could be considered. These obviously include no torsion effects either.

The following analysis essentially extends the Lyne (1970) results. In particular, it generalizes the steady streaming equations and derives an appropriate slip velocity

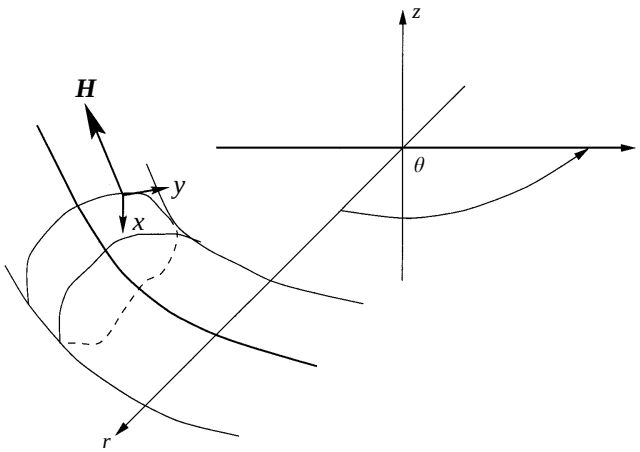

FIGURE 1. Helical coordinates r and $\phi = \theta + \varepsilon z$, with symmetry direction $\boldsymbol{H}$. The surface is given by $F(r, \phi) = 0$, and x and y (scaled in the boundary layer as X and Y) are in the directions of ∇F and $\nabla F \times \boldsymbol{H}$ respectively.

for helical flow which in the limit $\varepsilon \to \infty$ reduces to the Lyne problem. A purely oscillatory pressure gradient ($f(t) = \cos t$) is assumed.

As $\alpha \to 0$ with $R_s, R = O(1)$ kept constant, standard arguments suggest the core flow is inviscid at leading order and may be expanded as follows:

$$\left.\begin{aligned} v &\sim R_s(v_0 + \alpha v_1 + \ldots) \\ \Psi &\sim R_s(\Psi_0 + \alpha \Psi_1 + \ldots) \\ \xi &\sim R_s(\xi_0 + \alpha \xi_1 + \ldots) \end{aligned}\right\} \text{(core flow)}. \tag{3.1}$$

In the expansion (3.1) Ψ_0 and v_0 are of the same order as a consequence of (2.4) and the fact that the flow to leading order must be potential, forcing $\Psi_0 \neq 0$ (see ZM1). Since in the axisymmetric case ($\varepsilon \to \infty$) the cross-sectional flow is of smaller order than the primary flow, this is a consequence of non-zero torsion. In the following discussion, superscripts will be used to denote steady and unsteady parts so that, for example, $\Psi = \Psi^s + \Psi^u$. Substituting (3.1) into (2.7), (2.8) and (2.4), and equating like powers of α, one derives at leading order

$$\left.\begin{aligned} \frac{\partial v_0}{\partial t} &= \cos t, \\ \frac{\partial \xi_0}{\partial t} &= 0, \\ \mathscr{L}\Psi_0 &= \frac{2\varepsilon}{h^2} v_0 + \xi_0. \end{aligned}\right\} \tag{3.2}$$

In order to impose $\boldsymbol{u} = 0$ on the wall one has to consider the boundary layer equation. As follows from (2.7), (2.8) and (2.4), viscous terms can balance the pressure gradient on a scale of order α which determines the boundary layer thickness.

Now for a helical pipe with surface $S: F(r, \phi) = 0$, near the wall one can introduce coordinates (x, y) in the directions of ∇F, $\boldsymbol{H} \times \nabla F$ respectively, as in figure 1. Since x varies across the boundary layer it should be rescaled with α and it is convenient to normalize the coordinates so that inside the layer

$$X = x|\nabla F|\sqrt{2}/\alpha, \quad Y = y|\nabla F|\sqrt{2}. \tag{3.3}$$

This gives to leading order in α

$$\frac{\partial}{\partial r} \sim \frac{F_r}{\alpha\sqrt{2}|\nabla F|}\frac{\partial}{\partial X}, \quad \frac{\partial}{\partial \phi} \sim \frac{F_\phi}{\alpha\sqrt{2}|\nabla F|}\frac{\partial}{\partial X},$$

and

$$\mathscr{L} \sim \frac{1}{2\alpha^2}\frac{\partial^2}{\partial X^2} + \frac{1}{\sqrt{2}\alpha}\frac{F_r}{|\nabla F|}g(r)\frac{\partial}{\partial X} + O(1),$$

where

$$g(r) = \frac{1-\varepsilon^2 r^2}{rh^2}$$

and all the coefficients are evaluated on the boundary, i.e. vary only with y. The expected scalings in the boundary layer are

$$\left.\begin{aligned} v &\sim R_s(V_0 + \alpha V_1 \ldots) \\ \Psi &\sim R_s(\alpha\Phi_0 + \alpha^2\Phi_1 \ldots) \\ \xi &\sim R_s\left(\frac{\mathscr{E}_0}{\alpha} + \mathscr{E}_1 + \alpha\mathscr{E}_2 \ldots\right) \end{aligned}\right\} \text{(boundary layer).} \tag{3.4}$$

In (3.4), v in the boundary layer is of the same order as in the core so that as $x \to \infty$ it can match with its values in the interior. The vorticity ξ is of higher order inside the boundary layer, as required by an appropriate balance in equation (2.4), implying that $\mathscr{E}_0 \to 0$ as $X \to \infty$ and $\mathscr{E}_1$ matches with ξ_0 in the core, $\mathscr{E}_2$ with ξ_1 etc.

Substituting (3.4) into the governing equations gives the following balance in the boundary layer:

$$\left.\begin{aligned} \frac{\partial V_0}{\partial t} &= \cos t + \frac{1}{2}\frac{\partial^2 V_0}{\partial X^2}, \\ \frac{\partial \mathscr{E}_0}{\partial t} &= \frac{1}{2}\frac{\partial^2 \mathscr{E}_0}{\partial X^2}, \\ \frac{1}{2}\frac{\partial^2 \Phi_0}{\partial X^2} &= \mathscr{E}_0, \end{aligned}\right\} \tag{3.5}$$

with

$$\left.\begin{aligned} V_0, \Phi_0, \frac{\partial \Phi_0}{\partial X} &= 0 \quad \text{at} \quad X = 0, \\ |V_0|, \left|\frac{\partial \Phi_0}{\partial X}\right| &< \infty \quad \text{as} \quad X \to \infty, \\ \lim_{X\to\infty} \mathscr{E}_0 &= 0. \end{aligned}\right\} \tag{3.6}$$

The boundary conditions at $X = 0$ represent no-slip on the wall, while those as $X \to \infty$ appear as a consequence of matching. The problem (3.5), (3.6) has the solution

$$\left.\begin{aligned} V_0 &= \sin t - \mathrm{e}^{-X}\sin(t - X), \\ \mathscr{E}_0 &= U_0(Y)\mathrm{e}^{-X}\cos(t - X), \\ \Phi_0 &= U_0(Y)(\mathrm{e}^{-X}\sin(t - X) + (X - 1)\sin t), \end{aligned}\right\} \tag{3.7}$$

which matches with the core flow from (3.2)

$$\left.\begin{aligned} v_0 &= \sin t, \\ \xi_0 &= 0, \\ \mathscr{L}\Psi_0 &= \frac{2\varepsilon}{h^2}v_0, \quad \Psi_0 = 0 \text{ on } S. \end{aligned}\right\} \tag{3.8}$$

The function $U_0(Y)$ in (3.7) is the slip velocity defined by the first-order potential core flow, $U_0(Y)\sin t = \partial\Psi_0/\partial x$ on $x = 0$.

From (3.8) it follows that in the core at $O(\alpha)$ equations (2.7) and (2.8) read

$$\frac{\partial v_1}{\partial t} = 0 \quad \text{and} \quad \frac{\partial \xi_1}{\partial t} = 0 \tag{3.9}$$

so that $v_1^u = \xi_1^u = 0$ but $\Psi_1^u \neq 0$ as matching Φ_0 and Ψ_1 at $O(\alpha)$ in (3.7) implies Ψ_1^u satisfies the Dirichlet-type problem

$$\mathscr{L}\Psi_1^u = 0, \quad \Psi_1^u = -U_0 \sin t \quad \text{on} \quad S. \tag{3.10}$$

At second order, the boundary layer equations take the form

$$\left.\begin{aligned}
\frac{\partial V_1}{\partial t} - \frac{1}{2}\frac{\partial^2 V_1}{\partial X^2} &= -\frac{R_s}{r}J(\Phi_0, V_0) + \frac{1}{\sqrt{2}}\frac{F_r}{|\nabla F|}g(r)\frac{\partial V_0}{\partial X},\\
\frac{\partial \mathscr{E}_1}{\partial t} - \frac{1}{2}\frac{\partial^2 \mathscr{E}_1}{\partial X^2} &= -\frac{R_s}{r}J(\Phi_0, \mathscr{E}_0) - R_s\frac{2\varepsilon^2}{h^2}\frac{F_\phi}{\sqrt{2}|\nabla F|}\\
&\quad\times\left(\xi_0\frac{\partial \Phi_0}{\partial X} + V_0\frac{\partial V_0}{\partial X} - \frac{\varepsilon}{h^2}\frac{\partial^2 V_0}{\partial X^2} + \frac{g(r)}{\sqrt{2}}\frac{F_r}{|\nabla F|}\frac{\partial \mathscr{E}_0}{\partial X}\right),\\
\frac{1}{2}\frac{\partial^2 \Phi_1}{\partial X^2} - \mathscr{E}_1 &= \frac{2\varepsilon}{h^2}V_0 - \frac{F_r}{\sqrt{2}|\nabla F|}g(r)\frac{\partial \Phi_0}{\partial X}.
\end{aligned}\right\} \tag{3.11}$$

Since nonlinear terms have been included in (3.11), Φ_1, V_1 and $\mathscr{E}_1$ may have steady components. Using (3.7) one can obtain

$$V_1^s = \frac{R_s}{r}\det(Y)U_0'\left(-\tfrac{1}{4} - \tfrac{1}{4}\mathrm{e}^{-2X} + \frac{1}{\sqrt{2}}\mathrm{e}^{-X}\cos(X - \tfrac{1}{4}\pi) - \frac{1}{\sqrt{2}}\,X\mathrm{e}^{-X}\sin(X - \tfrac{1}{4}\pi)\right), \tag{3.12}$$

$$\begin{aligned}
\mathscr{E}_1^s = {}& \frac{R_s}{r}\det(Y)U_0U_0'\left(-\tfrac{1}{2}\mathrm{e}^{-2X} + \tfrac{1}{2}\mathrm{e}^{-X}\sin X - \mathrm{e}^{-X}\cos X + \frac{1}{\sqrt{2}}X\mathrm{e}^{-X}\cos(X - \tfrac{1}{4}\pi)\right)\\
&+R_s\frac{2\varepsilon^2}{h^2}\frac{F_\phi}{\sqrt{2}|\nabla F|}\left(-\frac{U_0^2+1}{4}\mathrm{e}^{-2X} - \tfrac{1}{2}\mathrm{e}^{-X}\sin X + \frac{1+U_0^2}{2}e^{-X}\cos X\right),
\end{aligned} \tag{3.13}$$

$$\begin{aligned}
\Phi_1^s = {}& \frac{R_s}{r}\det(Y)U_0U_0'\left(-\tfrac{1}{4}\mathrm{e}^{-2X} + \tfrac{1}{2}\mathrm{e}^{-X}\cos X - 2\mathrm{e}^{-X}\sin X\right.\\
&\left.-\frac{1}{\sqrt{2}}X\mathrm{e}^{-X}\sin(X - \tfrac{1}{4}\pi) + \tfrac{3}{2}X - \tfrac{1}{2}\right) + R_s\frac{2\varepsilon^2}{h^2}\frac{F_\phi}{\sqrt{2}|\nabla F|}\left(-\frac{U_0^2+1}{8}\mathrm{e}^{-2X}\right.\\
&\left.-\tfrac{1}{2}\mathrm{e}^{-X}\cos X - \frac{1+U_0^2}{2}\mathrm{e}^{-X}\sin X + \frac{U_0^2-1}{4}X - \frac{U_0^2-3}{8}\right).
\end{aligned} \tag{3.14}$$

In the above

$$\det(Y) = \frac{1}{2|\nabla F|^2}\frac{\partial(x, y)}{\partial(r, \phi)}$$

and the solution satisfies a non-slip boundary condition on the wall, i.e. V_0^s, Φ_1^s, $\partial\Phi_1^s/\partial X = 0$ on $X = 0$ while $\mathscr{E}_1^s \to 0$ as $X \to \infty$. The latter agrees with the first-order core solution given by (3.8) having no steady component since (3.7) and (3.13) as $X \to \infty$ imply there is nothing to drive such a steady flow.

Explicit formulae for Φ_1^u, V_1^u and $\mathscr{E}_1^u$ can also be found, as given in Zabielski (1996). For matching purposes, only their limits as $X \to \infty$ are required, when $V_1^u \to 0$ and

$\mathscr{E}_1^u \to 0$, agreeing with the core as given by (3.9), but

$$\Phi_1^u \sim -\frac{1}{\sqrt{2}}\frac{F_r}{|\nabla F|}g(r)U_0(Y)X^2\sin t + \frac{2\varepsilon}{h^2}X^2\sin t + G(t,Y)X + H(t,Y), \tag{3.15}$$

where $G(t,Y)$ and $H(t,Y)$ can be determined as below. Thus $\partial^2\Phi_1^u/\partial X^2$ is not zero on the edge of the boundary layer and must agree with $\partial^2\Psi_0/\partial x^2$. Since $\Psi_0 = 0$ and $\partial\Psi_0/\partial x = U_0(Y)\sin t$ on S, the third equation in (3.8) takes the following form on the boundary S:

$$\frac{\partial^2\Psi_0}{\partial x^2} + \frac{1}{\sqrt{2}}\frac{F_r}{|\nabla F|}g(r)U_0\sin t = \frac{2\varepsilon}{h^2}\sin t. \tag{3.16}$$

From (3.15) and (3.16) it follows that as $X \to \infty$ and $x \to 0$, $\frac{1}{2}\partial^2\Phi_1^u/\partial X^2 = \partial^2\Psi_0/\partial x^2$. The function $G(t,Y)$ in (3.15) is matched with $U_1(Y)\sin t \equiv \partial\Psi_1^u/\partial x$ on S, ensuring the tangential velocities agree at the edge of the layer. Now if the boundary conditions $\Phi_1^u, \partial\Phi_1^u/\partial X = 0$ are imposed on $X = 0$, then $\mathscr{E}_1^u$ can be fully determined, and the unknown function $H(t,y)$ found. The latter then matches with Ψ_2^u in the core.

In order to determine v_1^s, ξ_1^s in the core one must first establish the time-dependent behaviour of higher-order terms. Taking (3.8) and (3.9) into account, at $O(\alpha^2)$,

$$\left.\begin{aligned} \frac{\partial v_2}{\partial t} + \frac{R_s}{r}J(\Psi_0, v_1^s) &= 0,\\ \frac{\partial\xi_2}{\partial t} + R_s\left(-\frac{2\varepsilon}{h^2}\frac{1}{r}J(\Psi_0,v_1^s) + \frac{1}{r}J(\Psi_0,\xi_1^s) + \frac{2\varepsilon^2}{h^2}\xi_1^s\frac{\partial\Psi_0}{\partial\phi} + v_0\frac{\partial v_1^s}{\partial\phi}\right) &= 0,\\ \mathscr{L}\Psi_2 &= \frac{2\varepsilon}{h^2}v_2 + \xi_2. \end{aligned}\right\} \tag{3.17}$$

Since $\Psi_0, v_0 \sim \sin t$, it follows that the unsteady terms $v_2^u, \xi_2^u \sim \cos t$. Taking the steady component of the core equations at $O(\alpha^3)$, one can derive the following:

$$\left.\begin{aligned} \frac{1}{r}J(\Psi_1^s, v_1^s) &= \frac{R}{R_s} + \frac{1}{R_s}\left(\mathscr{L}v_1^s + \frac{2\varepsilon}{h^2}\xi_1^s\right),\\ \frac{1}{r}J(\Psi_1^s,\xi_1^s) + \frac{2\varepsilon^2}{h^2}\left(\xi_1^s\frac{\partial\Psi_1^s}{\partial\phi} + v_1^s\frac{\partial v_1^s}{\partial\phi}\right) &= \frac{2\varepsilon}{h^2}\frac{R}{R_s} + \frac{1}{R_s}\mathscr{L}\xi_1^s,\\ \mathscr{L}\Psi_1^s &= \frac{2\varepsilon}{h^2}v_1^s + \xi_1^s. \end{aligned}\right\} \tag{3.18}$$

Note that terms such as $J(\Psi_0, v_2^u)$ have no mean for pressure gradients with $f(t) = \cos t$, and hence do not appear in (3.18). This is true for functions $f(t)$ with the symmetry $f(t+\pi) = -f(t)$ for which the analysis easily extends, but in general (3.18) can be more complicated.

The solution to (3.18) must match with $V_1^s, \partial\Phi_1^s/\partial X$ in the boundary layer. Using (3.12)–(3.14) this defines, finally, the following boundary conditions for the steady core flow:

$$\left.\begin{aligned} v_1^s &= -\frac{R_s}{4r}\det(Y)U_0',\\ \frac{\partial\Psi_1^s}{\partial x} &= R_s\frac{2\varepsilon^2}{h^2}\frac{F_\phi}{|\nabla F|}\frac{U_0^2-1}{4} + \frac{3\sqrt{2}R_s}{2r}\det(Y)U_0U_0',\\ \Psi_1^s &= 0. \end{aligned}\right\} \tag{3.19}$$

Comparison with equation (4.1) of ZM1 indicates that equation (3.18) for the leading-order steady core flow is precisely the steady Navier–Stokes equation, with, however, a prescribed slip velocity given by (3.19). This steady flow is driven partly by the mean

component of the pressure gradient (R) and partly by the second-order interaction of unsteady terms. The boundary condition (3.19) ensures that the core flow will have a steady component even when $R = 0$, when it is totally controlled by steady streaming from the boundary layer as found in the axisymmetric case by Lyne (1970). When $R \neq 0$, the interaction between steady streaming and a mean pressure gradient down the pipe can be studied. This problem was considered by Blennerhassett (1976) for the axisymmetric case and non-uniqueness of the solution was discovered in some parameter ranges. The axisymmetric results may be derived from the helical case in the limit $\varepsilon \to \infty$. For example, if $R = 0$, as $\varepsilon \to \infty$ one obtains $\Psi_0 = 0$ which gives $U_0 = 0$ on the boundary. This simplifies the formulae (3.12)–(3.14) so that (3.19) yields

$$v_1^s = 0, \quad \frac{\partial \Psi_1^s}{\partial x} = -\frac{1}{2}\frac{R_s}{r}\frac{F_\phi}{|\nabla F|}. \tag{3.20}$$

After the further small curvature limit ($a/b \to 0$, so that r is constant to leading order), the Lyne (1970) steady streaming slip velocity for a circular cross-section $\partial \Psi / \partial x = -\frac{1}{4} R_s \sin y$ is obtained. (Note that Lyne performed the analysis with respect to the small parameter $\beta = \sqrt{2}\alpha$.) In this limit, Lyne showed that the equation for Ψ_1^s with boundary condition (3.20) is the two-dimensional Navier–Stokes equation.

Interestingly, if we take the two-dimensional limit ($\varepsilon \to 0$) in (3.19), we obtain a mathematically equivalent problem for Ψ_1^s as in the low-curvature, axisymmetric Lyne analysis, while again $v_1^s \to 0$. This suggests that the structure of the steady flow is identical in the limits of firstly two-dimensionality ($\varepsilon \to 0$) and of secondly low-curvature axisymmetry (b, $\varepsilon \to \infty$). One may therefore postulate that a qualitatively similar picture will emerge for the steady cross-pipe flow at any finite ε, provided the curvature is small, and the numerical results of §4 bear this out. The core surface velocity, U_0, is found to be notably smaller than unity even when $\varepsilon = O(1)$, so that often the difference between (3.19) and (3.20) is not so large. However, in the helical case there exists a torsion-driven steady flow component down the pipe ($v_1^s \neq 0$). If S is circular, then $v_1^s < 0$ in the top of the pipe, and $v_1^s > 0$ below, so that fluid drifts down the top of the pipe and up the bottom. This, and other three-dimensional effects are discussed below.

3.1. *Torsion effects*

If $R = 0$, the flow as defined by (2.4), (2.7) and (2.8) is driven by an oscillating pressure gradient with no mean component. For general ε, unsteady cross-pipe motion is generated at leading order with respect to α. This flow is not present in axisymmetry and is asymptotically larger than the cross-pipe flow generated by the steady streaming effect. In the helical case, as well as the steady streaming given by (3.18) and (3.19), the second-order perturbation now also has an oscillatory part, as follows from (3.10).

The primary flow down the pipe also has a different asymptotic structure compared to that in axisymmetry. In the limit $\varepsilon \to \infty$ the governing equations are symmetric with respect to the plane $z = 0$ and the secondary, cross-pipe motion always has a two-vortex pattern. When the pressure gradient changes its direction this affects the primary flow, basically changing its direction, while the secondary motion remains the same. This implies that the down-pipe flow may not have a steady component simply because there is no preferential direction for such a motion. The second-order perturbation affects only the cross-pipe motion, and is steady in the core Lyne (1970). For finite ε, as the pressure gradient changes its direction then in the governing

equations (2.7) and (2.8)

$$\phi \to -\phi, \quad v \to -v, \quad \Psi \to -\Psi, \quad \xi \to -\xi. \tag{3.21}$$

This means that the flow down the pipe reverses and the cross-pipe motion has a bottom-top symmetry with respect to ϕ. The change in direction of the pressure gradient is equivalent to taking the pipe S_- : $F(r, -\phi) = 0$ instead of S.

If the helical pipe is symmetric in ϕ, i.e. $S_- = S$, the opposite gradient generates essentially the same helical flow. This implies in particular that the flow generated by the steady streaming effect (3.18), (3.19) with $R = 0$ carries no net flux, as (3.21) implies $v(r, \phi) = -v(r, -\phi)$.

The situation is quite different when $S \neq S_-$ and the helical pipe is not top-bottom symmetric. Then from the point of view of the pressure gradient, S and S_- represent different boundaries and the opposite pressure gradient may give rise to a completely different motion. In particular, the induced steady flow may involve a non-zero flux down the pipe, even though there is no mean pressure gradient, which can be regarded as geometrical pumping. Since in the limit $\varepsilon \to \infty$ flows in S and S_- are the same, this is a purely three-dimensional effect.

3.2. *The wall shear stress*

In the Stokes boundary layers, the wall shear stress σ is proportional to the velocity jump across the layer, and to leading order it can be found from (3.7) and the potential problem (3.8). Such a problem was solved in ZM1 for a rectangular cross-section. Importantly, the potential core flow has components in all directions, and thus in a physiological context, the cleansing action of the shear on arterial walls is arguably more efficient. It is convenient to decompose the stress into two parts $\sigma = \sigma_\Psi + \sigma_H$ where σ_Ψ, σ_H are generated respectively by the velocity of the cross-pipe and down-pipe flows.

Numerical calculation shows that the down-pipe stress component σ_H is not particularly affected by the torsion. Its distribution is more or less determined by the curvature, and is maximum near the inside of the bend. The situation is different for the cross-pipe component, σ_Ψ, which is zero in the limiting cases $\varepsilon \to 0, \infty$. As ε is decreased from infinity, σ_Ψ reaches a maximum at $\varepsilon \simeq a/b$. For this particular value of the parameter ε the helical pipe is stretched to its maximum torsion at a given curvature. For all values of $\varepsilon > a/b$, σ_Ψ has its maximum at the inner part of the bend. For $\varepsilon < a/b$, the torsion dominates the curvature and the maximum of σ_Ψ moves towards the outside of the bend as the two-dimensional limit is approached.

When the two parts of the shear stress are superposed, however, the maximum magnitude of the stress vector remains near the inside of the bend for all values of ε as the torsion effects are too uniform to destroy the distribution induced by the curvature.

The wall stress is oscillatory at leading order, but it also has a steady component which can be found from the steady streaming problem (3.18). From a physiological point of view, the absolute magnitude of the stress, its spatial variation and its time-average are all significant. In a real artery, of course, the driving pressure pulse is not sinusoidal, and a numerical approach is necessary for general $f(t)$.

4. The numerical approach

In the preceeding section, the asymptotic structure of the flow driven by a simple oscillating pressure gradient in the high-frequency limit was found. It was necessary

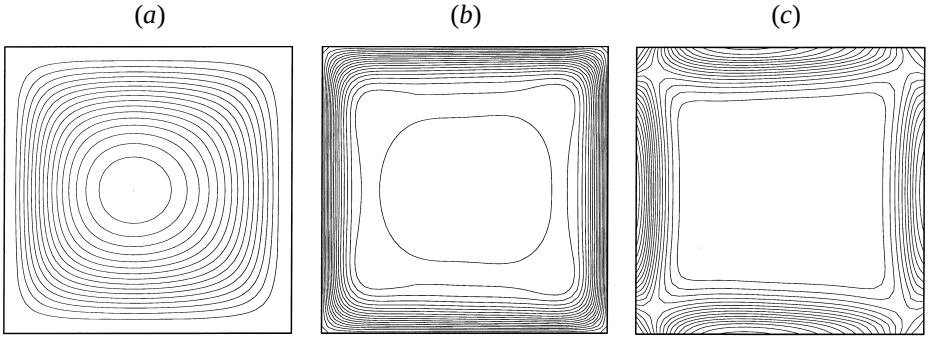

FIGURE 2. Coefficient of $\sin t$ for $f(t) = \cos t$, $R_s = 1$, $\alpha = 0.05$. (*a*) Ψ; (*b*) v; (*c*) ξ. The inside of the bend is on the left.

to assume $R_s\alpha \ll 1$ so that the leading-order problem was linear. As R_s increases towards physiologically relevant values, the asymptotics of § 3 cease to be valid, and the nonlinear problem requires numerical treatment. Likewise, if a more complicated pressure pulse is considered, while the above arguments could be generalized, in practice a numerical approach is advisable. The range of validity of the asymptotic solution can also be found numerically.

In the present work finite difference schemes for the time-dependent, helically symmetric Navier–Stokes equation were developed allowing for an arbitrary pressure gradient. Rectangular and circular geometries were considered, while the imposed pressure gradient was either sinusoidal or physiological.

Two alternative centred schemes were developed, one explicit and one implicit using the three-time-level scheme described by Fletcher (1991). These are used to step the equations (2.7) and (2.8) forward in time. Each time step a Gauss–Seidel routine is applied to the elliptic problem (2.4) using a block method Strikwerda (1989). The no-slip condition is then used to update the surface vorticity. The computation is continued until a fully developed, time-periodic state is reached. As some solutions exhibit separation and internal shear layers it was considered advisable to use a uniform grid. The code was shown to have the expected second-order spatial behaviour by comparing solutions on differing grids, as described in ZM1. The solutions agree with the asymptotics of the previous section for small α and R_s.

For large values of R_s the computational cost is much higher than for the steady case considered in ZM1. The results obtained for the highest values of R_s considered below have not, therefore, been compared with solutions on yet finer grids, but their convergence behaviour is convincingly robust. It is possible that a periodic solution could be found more efficiently than by the chosen method of direct time evolution. However, the development of aperiodic solutions or of other instabilities might be concealed by such an approach. The solutions found by the described approach should at least be stable to any helically symmetric disturbance.

4.1. *Rectangular pipe*

In the (r, ϕ)-plane the pipe cross-section is taken to be the rectangle $0 \leqslant \phi \leqslant \phi_0$, $b - a \leqslant r \leqslant b + a$, so that the boundary consists of (r, ϕ) coordinate surfaces. In this case it is particularly easy to impose the boundary conditions on the wall so that a finite difference scheme can be implemented using (r, ϕ) variables.

For the cases below, a pressure gradient $f(t) = \cos t$ is used with $R = 0$. The helical pitch is chosen to be $\varepsilon = 1$, while the other geometrical parameters are $a = 0.5$,

$b = 1.5$ and $\phi_0 = 1$. The flow is controlled by the amplitude parameter R_s and the Womersley number α^{-1}. In the present study, the Womersley number will be set to the physiologically relevant value $\alpha = 0.05$, so that the solution behaviour depends only on R_s. For fixed α, the parameter R_s measures the relative magnitude of the nonlinear terms compared with the viscous forces and thus represents a Reynolds number for the problem. Computations have been carried out in the range of $R_s = 1$–$60\,h_b$. For small values of R_s ($R_s < 10\,h_b$) the obtained numerical solution is in good agreement with the small-α asymptotics of the previous section. In figure 2, the first sine-harmonic of the numerical solution is shown. The contours of the streamfunction are almost identical to those of the solution of the potential problem (3.8) as plotted in figure 3 of ZM1. The almost constant down-pipe core velocity is also as predicted by the asymptotic model. The other terms in the Fourier decomposition are much smaller; roughly 10–15% of the dominant term. Hence, the picture in figure 2 is seen throughout the time cycle except close to the flow reversal at $t = n\pi$.

As R_s is increased above the value $20\,h_b$, so that $R_s\alpha = O(1)$, the nonlinear terms become important and the previous analyses are no longer valid. Individual Fourier modes then give a poor description of the flow and in order to follow the time evolution it is necessary to refer directly to different instants in time. Since $t \to t + \pi$ implies $f(t) \to -f(t)$, from (3.21) the corresponding flow patterns should be antisymmetric in ϕ. This is indeed observed in numerical simulations for $R_s \leqslant 20\,h_b$ and one need consider but half of the time cycle. However, the situation is quite different when $R_s = 30\,h_b$. Then, the computed solution is not invariant with respect to (3.21) which leads to the conclusion that uniqueness has been lost and a bifurcation has occurred. This phenomenon will be discussed below. When R_s is increased to $40\,h_b$ the (3.21) invariant solution is obtained again and for all the higher values considered ($R_s = 50\,h_b, 60\,h_b$) qualitatively the same structure is observed. A typical flow pattern at the relatively high $R_s = 60\,h_b$ is shown in figure 3. The secondary motion consists of two vortices which change their size and interact during the time evolution, pushing each other into respectively the upper and lower corners at the outer wall. This is illustrated by the contours of the streamfunction Ψ plotted at various time instants. The primary flow velocity v behaves in a fairly complicated manner. Since the value of R_s is quite large some functional dependence between Ψ and v can be expected ($v \simeq v(\Psi)$ – see ZM1) and this can indeed be observed. Near the beginning of the cycle ($t = 0$) the vorticity ξ is mostly accumulated within the thin boundary layer at the top wall while at the bottom it is rather diffused and fairly constant in the core. As $t \to \pi$, the region of large ξ moves from the top to the bottom of the rectangular pipe and two almost symmetric regions are formed near $t = \pi/2$. At this time instant the velocity v is fairly uniform in the core and the secondary flow vortices are of roughly the same size. Around $t = 5\pi/6$ the flow starts reversing and v changes sign first at the inner wall.

Since the problem is nonlinear a steady flow component is generated for all values of R_s which increases in strength with R_s as nonlinear behaviour becomes dominant. However, as $R_s \to \infty$ there is no obvious relation between v^s and Ψ^s, although $v \simeq v(\Psi)$ at any time instant.

4.2. *Circular pipe*

Numerical simulations of unsteady helical flow inside a circular pipe require more effort compared to a rectangular geometry, because the boundary is not a natural coordinate line. The coordinate system used is described in ZM1, as is the method of dealing with the coordinate singularity.

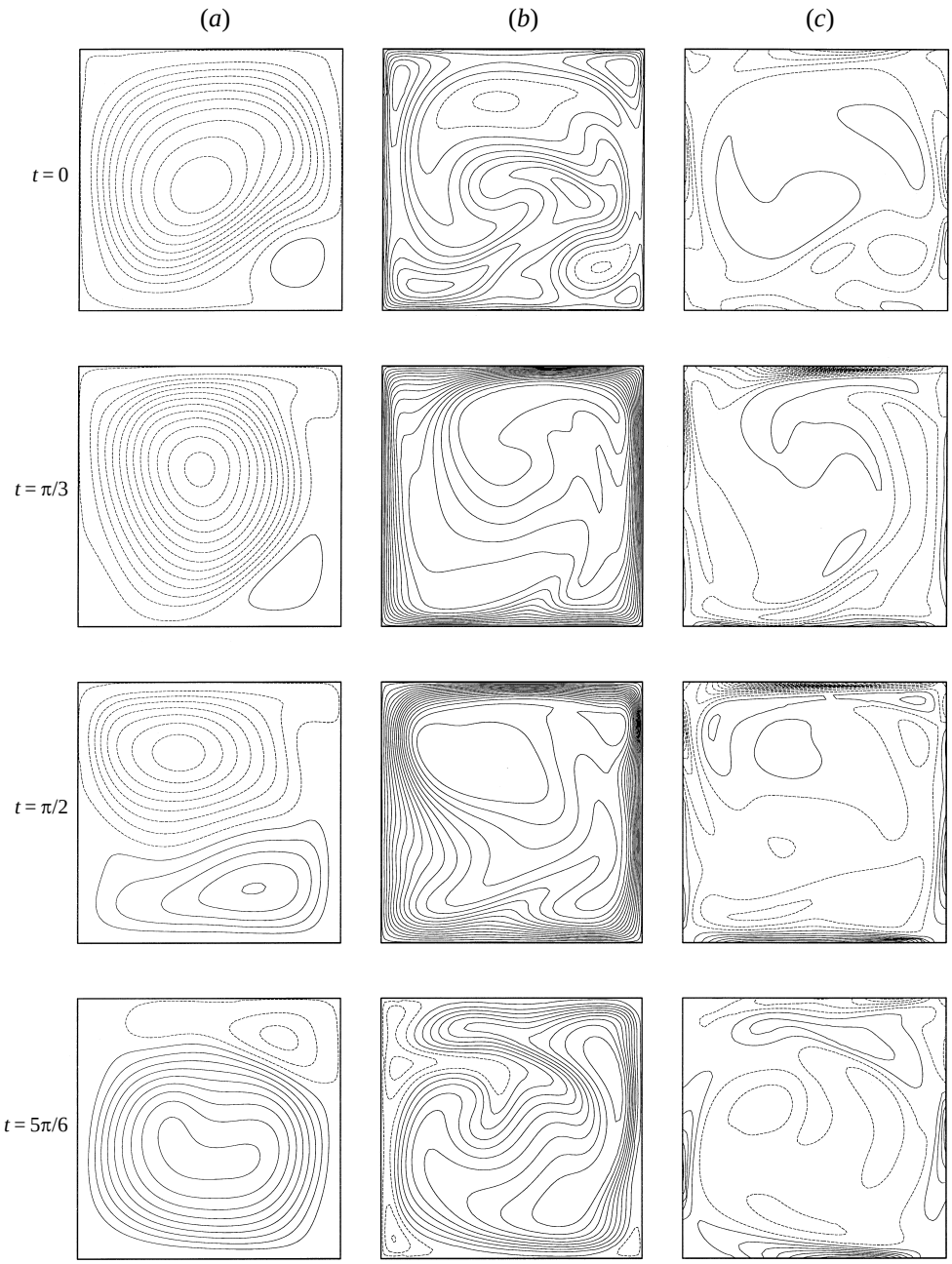

FIGURE 3. Flow for $f(t) = \cos t$ for $R_s = 60\,h_b$ and various time instants. (*a*) Ψ; (*b*) v; (*c*) Ψ. The reversal of the flow can be seen from the negative broken lines and the positive solid lines. The inside of the bend is on the left.

Just as for a rectangle, unsteady helical flow driven by a simple harmonic of the pressure gradient $f(t) = \cos t$ with no mean component ($R = 0$) was studied. The pipe radius $a = 1$ and in all the simulations the physiological value of the Womersley number $\alpha = 0.05$ was used. Solutions have been obtained for various values of R_s and the curvature (b) and torsion (ε) of the helical pipe. For $R_s < 10\,h_b$ the asymptotic

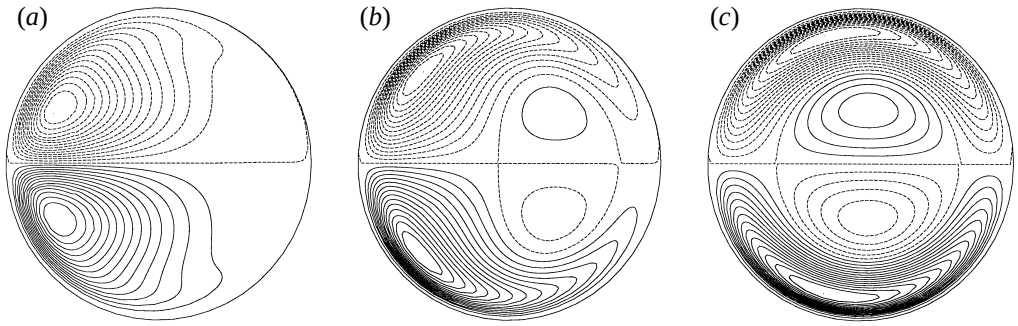

FIGURE 4. Effect of curvature (neglected by the Dean approximation) on the steady flow component in axisymmetry ($\varepsilon = 100$). (*a*) $b = 1.2$; (*b*) $b = 2$; (*c*) $b = 10$. The inside of the bend is on the left.

structure in the limit $\alpha \to 0$ has proved to be valid and flow patterns qualitatively the same as in the rectangular case (figure 2) have been found. The behaviour observed in this parameter regime ($R_s\alpha \ll 1$), however, is determined by the linearized equations of motion so that not all of the important flow characteristics are exhibited. In order to get a more complete understanding higher-order perturbations in α were considered in § 3, which we now compare with the numerical solutions.

An effect entirely due to the nonlinearity is the driving of a steady motion, even in the case of no steady pressure gradient ($R = 0$). According to the asymptotic analysis such a flow results from steady streaming from the boundary layer at second order in α. This small effect nevertheless dominates the cross-pipe flow in the axisymmetric limit $\varepsilon \to \infty$ when the unsteady part of Ψ is zero at leading order and the potential core retains only a down-pipe component Lyne (1970). The most important characteristic of Lyne's solution is a steady, cross-pipe motion which in the core is directed from the outer to inner wall, i.e. in the opposite sense to the classical Dean pattern for a steady pressure gradient. The steady component of the flow can easily be separated numerically and the behaviour for different parameter values can be studied. As $\varepsilon, b \to \infty$ the case considered by Lyne is approached and the contours of the steady part of the streamfunction Ψ obtained for $\varepsilon = 100$ and $b = 1.2, 2, 10$ are shown in figure 4. For $b = 10$ the asymptotic structure of the Lyne solution is pronounced. In the centre of the pipe two recirculating regions which redirect the flow from the outer to inner bend have developed and centrifugally driven Dean-type vortices appear only inside the Stokes boundary layers at the top and bottom. It should be pointed out that this solution has been obtained numerically by solving the full nonlinear equations of motion (with helical symmetry) which lends particularly strong support to Lyne's asymptotic analysis. However, it was found numerically that the steady flow pattern may be quite different in the presence of strong curvature. As b is decreased the steady streaming vortices become much smaller and move towards the outer bend. At the same time, the contours of the Dean-type flow are pulled from the boundary layer into the centre of the pipe (figure 4, $b = 2$). Hence for b very close to unity, a flow directed toward the outer bend is dominant in most of the axisymmetric cross-section (figure 4, $b = 1.2$). For the particular values $a = 1$, $\alpha = 0.05$, these results seem to suggest that the steady streaming vortices appear only in the region of the pipe for $r > 2$.

In the helical case when ε is arbitrary, steady streaming was shown to be governed by the equations (3.18) with the boundary condition (3.19). In § 3 it was suggested that the steady streaming effect would be fairly insensitive to variations in ε. This is

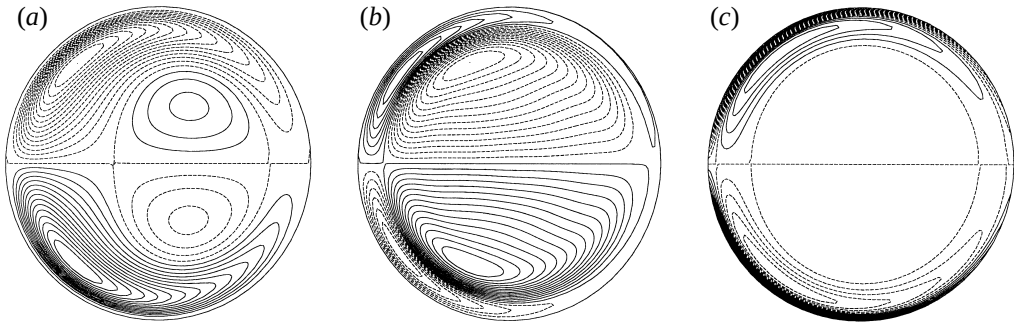

FIGURE 5. Steady component of the flow for $\varepsilon = 1$, $b = 2$, $R_s = 1$. (*a*), Ψ, (*b*) v, (*c*) ξ. The cross-pipe flow is markedly similar to axisymmetric flow. Additionally, the fluid flows up the bottom and down the top of the pipe. The inside of the bend is on the left.

borne out by the numerical calculations. Figure 5 shows the steady component of the periodic flow for $\varepsilon = 1$, $b = 2$ and $R_s = 1$. The Ψ-contours bear a marked similarity with the axisymmetric solution in the middle of figure 4 with $b = 2$. Also, as predicted by the analysis, a steady flow up and down the pipe develops which is antisymmetric in ϕ so that the total flux is zero.

Again, as $\varepsilon \to 0$, good agreement with the asymptotic results is found. As ε is decreased, the curvature becomes small so that steady streaming vortices can appear in the centre of the pipe. Thus a flow pattern similar to that in axisymmetry with large b is formed (figure 4, $b = 10$) as discussed in § 3. In general, one can conclude that torsion does not have a particularly important effect on steady streaming which is affected in a much greater way by strong curvature.

4.2.1. *Symmetry breaking*

Helical flow driven by a purely oscillatory pressure gradient ($R = 0, f(t) = \cos t$) is expected to be antisymmetric in ϕ when $t \to t + \pi$, as in (3.21). For some parameter values, however, numerical solutions which are not invariant with respect to this transformation have been obtained. For example, see figure 6 ($R_s = 20\,h_b$, $\varepsilon = 1, b = 2$) at $t = 0, \pi$. This leads to the conclusion that uniqueness has been lost and a symmetry-breaking bifurcation has occurred. Certainly the symmetry (3.21) could easily be imposed in the numerical studies and another solution at $R_s = 20\,h_b$ would then presumably be found. Then, using these two flows as starting conditions and gradually increasing or decreasing the parameter R_s, different branches could be followed and a global bifurcating structure could be investigated. However, the computational effort to find a time-periodic solution at large R_s is non-trivial as large number of points are required to resolve the boundary layers while the slow viscous diffusion implies that many time steps are necessary to achieve a fully developed time-periodic flow. In the present work it was not felt worthwhile to investigate the bifurcation structure in detail, and some of the following comments must therefore be regarded as speculative and incomplete.

Non-symmetric solutions were found for both the rectangular and circular cases in the parameter window $R_1 < R_s < R_2$ with $R_s\alpha = O(1)$. Thus, as R_s was increased, symmetric solutions were found for $R_s > R_2$ and the same occurred also for $R_s < R_1$. For no parameter values were two essentially distinct solutions found, although this was not investigated in depth. It is probable that the symmetry breaking occurs as a super-critical pitchfork bifurcation. The disappearance of the asymmetric solution is

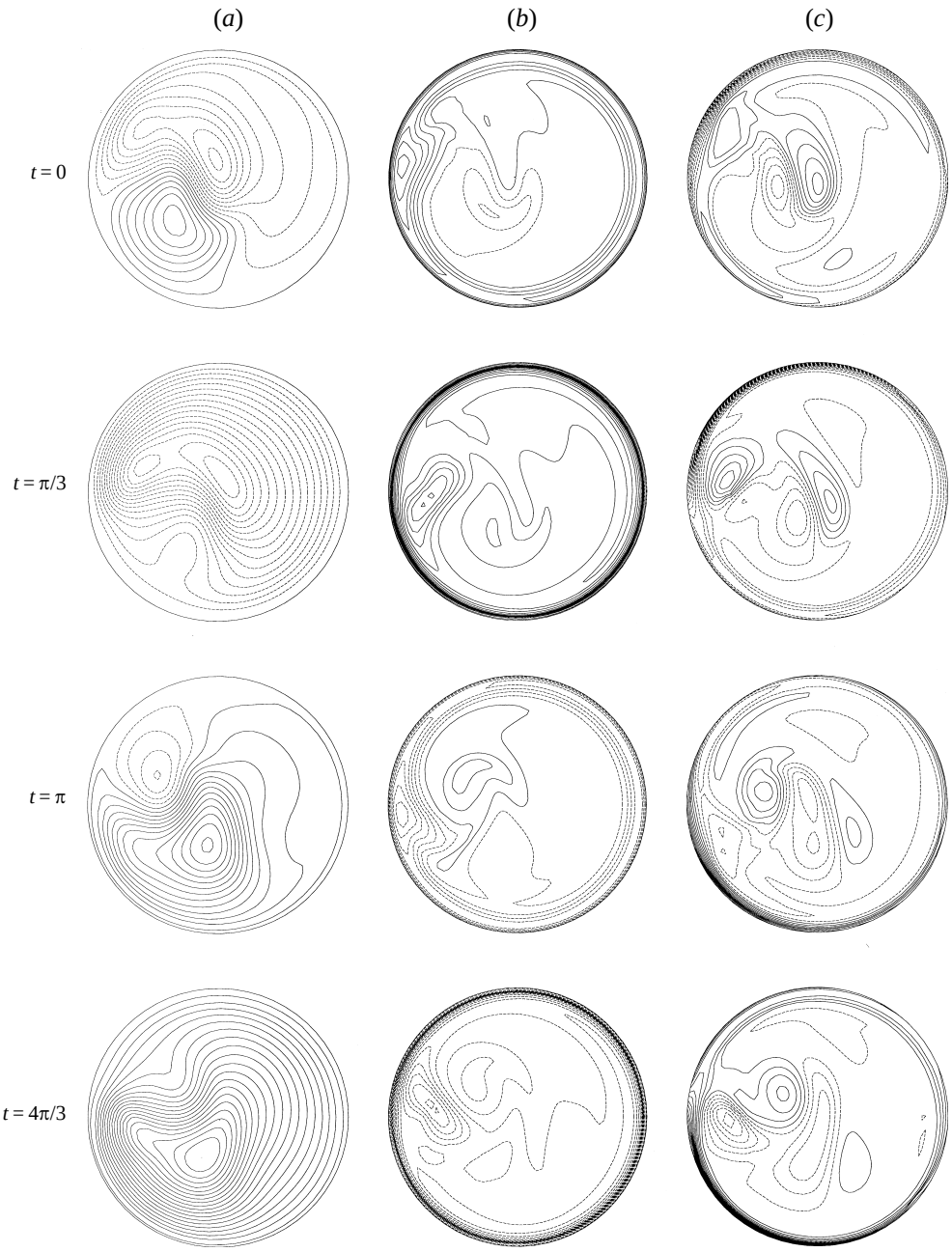

FIGURE 6. Symmetry breaking for $f(t) = \cos t$, $\varepsilon = 1$, $b = 2$, $R_s = 20\,h_b$. (*a*) Ψ, (*b*) v, (*c*) ξ. Compare $t = 0, \pi$ and $t = \pi/3,\ 4\pi/3$. The inside of the bend is on the left.

presumably associated with the symmetric solution regaining stability. Whether the asymmetric solution ceases to exist for $R_s > R_2$ as in Moore, Weiss & Wilkins (1990), becomes unstable, or exists but has simply not been found, is uncertain. It should be remembered that the numerical method would not find helically unstable solutions. A plausible conjecture may be that non-uniqueness only occurs when $R_s\alpha = O(1)$, when

the inertial term, the time derivative and the pressure gradient are all of comparable size.

For spatially asymmetric pipes ($S \neq S_-$) or temporally asymmetric pressure pulses such as the physiological $f(t)$ (figure 8 below) the bifurcation would be harder to detect.

4.2.2. *Flow at high R_s*

At $R_s = 40\,h_b$, the highest value considered, a solution symmetric in the sense of (3.21) has been obtained and various time instants are shown in figure 7. The flow is quite complicated in this case, the cross-pipe motion consisting of three recirculating regions which rotate around the centre of the pipe, changing their size and orientation in time. The down-pipe velocity v is fairly uniform in the interior with quite strong gradients near the boundary. At the beginning of the time cycle ($t = 0$) the vorticity accumulates in the region near the wall at the top and during the time evolution, just as for the rectangle, a high-shear region develops on the bottom of the pipe as $t \to \pi$. At $t = 2\pi/3$ the flow starts reversing and strong separation is noticeable at the inner wall. A jet-like structure emerges, forming a pair of counter-rotating ξ-vortices at the bottom of the pipe. The expected functional dependence $v \simeq v(\Psi)$ is visible and to an extent this is the case for the steady components (not shown) also. The structure of the steady cross-pipe motion is qualitatively similar to that in figure 5 ($R_s = 1$), although it is larger at high R_s. Up to a point, the Ψ contours in figure 7 can be viewed as a superposition of a steady flow and a first sine-harmonic, although this is of course a gross simplification of the nonlinear flow.

4.3. *Pulsatile (physiological) flow*

Although helical symmetry simplifies the governing equations and permits study of non-planar geometry, the resulting flow is fully developed and requires the pipe to be sufficiently (infinitely) long. Such an assumption in particular does not allow for any transient structures which would normally appear in the flow near the entrance to or exit from the pipe. Nevertheless, if the oscillation period is short compared to the fluid transit time in the relevant arterial portion, a fully developed model should be reasonable. Furthermore, the geometrical parameters b, ε are arbitrary and can be chosen to fit a particular geometry, while the form of the pressure gradient, $f(t)$ in (2.5), may be taken directly from experiment.

In physiological applications the blood flow is driven by the heart beat which corresponds to a pulsatile periodic forcing with relatively small mean component. The generic cases of steady and oscillating, sinusoidal flows have been studied in ZM1 and the previous sections. Yet for the macro-circulation in the body $R_s\alpha > 1$ and the nonlinear terms are significant. Thus the flow patterns for individual Fourier modes cannot simply be superposed and their interaction needs to be investigated. Phenomena such as steady streaming and centrifugal secondary motion can appear simultaneously within the flow field. The steady component of the resulting flow carries all of the mass flux around the arterial system, so that even when it is small compared to the oscillating part it still controls the entire circulation in the body.

In numerical simulations, instead of the mean part with only a single time-harmonic one may just as well use a full physiological pressure pulse which is available from experimental studies. The function $f(t)$, shown in figure 8, is obtained from McDonald (1974), based on measurements inside the canine femoral artery. The time-dependence of the pressure gradient can certainly vary from subject to subject and with distance from the heart, so that the pulse in figure 8 is different in other parts of the body and

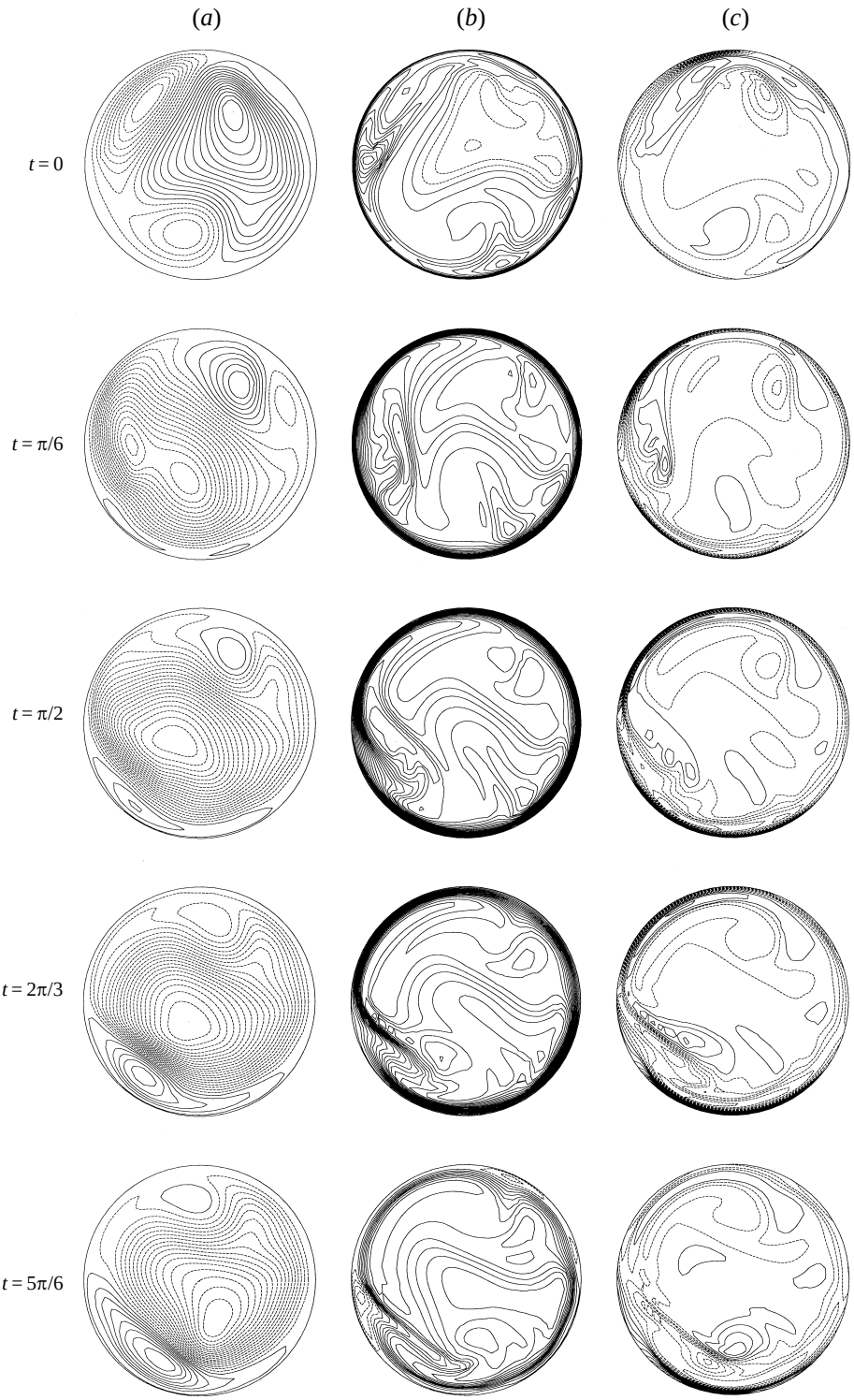

FIGURE 7. Symmetric solution for $f(t) = \cos t$, $R_s = 40\,h_b$. (*a*) Ψ, (*b*) v, (*c*) ξ. Strong separation from the inner bend (on the left) near flow reversal (dotted lines are negative).

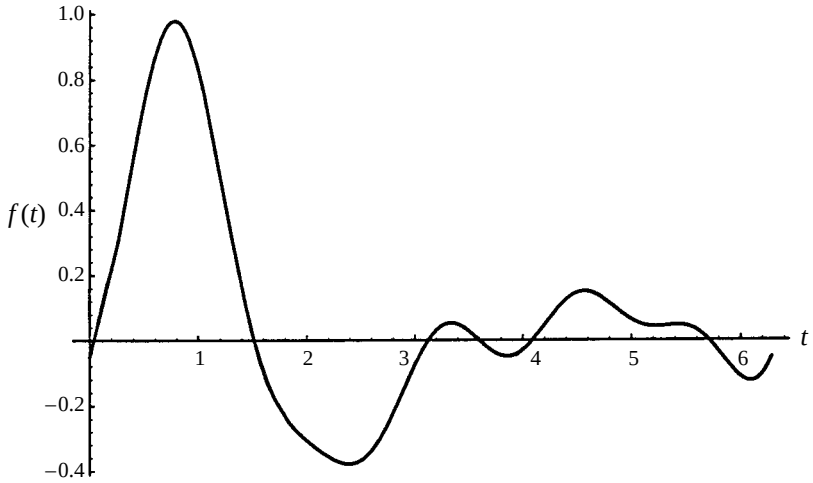

FIGURE 8. Measured physiological pressure gradient (McDonald 1974).

even more so in the human arterial system. Nevertheless, the general characteristic of a large peak in the first half of the time-cycle called systole and a fairly steady behaviour in the second usually referred to as diastole, remains unchanged. The main difference is that the profile is somewhat flatter in the arteries far from the heart. Hence, since the present work is primarily concerned with qualitative flow structures and the effect of geometry, the function $f(t)$ in figure 8 will be treated as the shape of a general physiological forcing which needs only to be appropriately rescaled with R_s and R in order to represent typical conditions inside a given arterial bend. For example, parameters appropriate to the aortic arch, the major three-dimensional bend in the body, are $a/b = 0.4$, $\alpha = 0.05$, $D = 600$ Chandran (1993). In the present scalings, as given by (2.9), this is equivalent to $b = 2$ and $R = 950\,h_b$. The relevant values of R_s can be estimated based on the Lyne (1970) steady streaming number which for the canine aorta is 4200 Pedley (1980). As this corresponds to $a/b = 0.2$ and $\alpha = 1/13$, it can be deduced that for the human circulation the range $R_s = 75\,h_b$–$100\,h_b$ is appropriate. When all these parameter values are substituted and $f(t)$ is prescribed as in figure 8, the balance achieved between different terms in the governing equations is arguably the same as that determined by the blood flow inside the aortic arch. Hence the effect of torsion in the physiological context can be studied.

Computations have been carried out for the case $b = 2, \alpha = 0.05, R = 950\,h_b$, $f(t)$ as in figure 8 and solutions have been obtained for various values of ε and R_s. When R_s is small ($R_s < 30\,h_b$), as expected, all the Fourier modes separate and the behaviour is essentially the same as in the asymptotic limit $\alpha \to 0$ (compare figure 2). Such a solution, however, requires $\alpha R_s < O(1)$ which certainly is not satisfied in the physiologically relevant parameter regime when the nonlinear terms seem rather to dominate. In figure 9 flow patterns for the fairly realistic conditions $R_s = 80\,h_b$, $\varepsilon = 1$ corresponding to those inside the human aortic arch are shown. In this case, although the flow is quite complex and involves much nonlinear interaction, a typical time profile still follows, to an extent, the shape related to $f(t)$ in figure 8. The secondary motion is most of the time of one-vortex type and it becomes especially strong near the systolic peak (figure 9, $t = 2\pi/6, 4\pi/6$) while during diastole it seems to be rather trapped near the bottom of the inner bend (figure 9, $t = 7\pi/6$). The latter behaviour is reflected in the contours of the primary velocity v which separate from the wall in

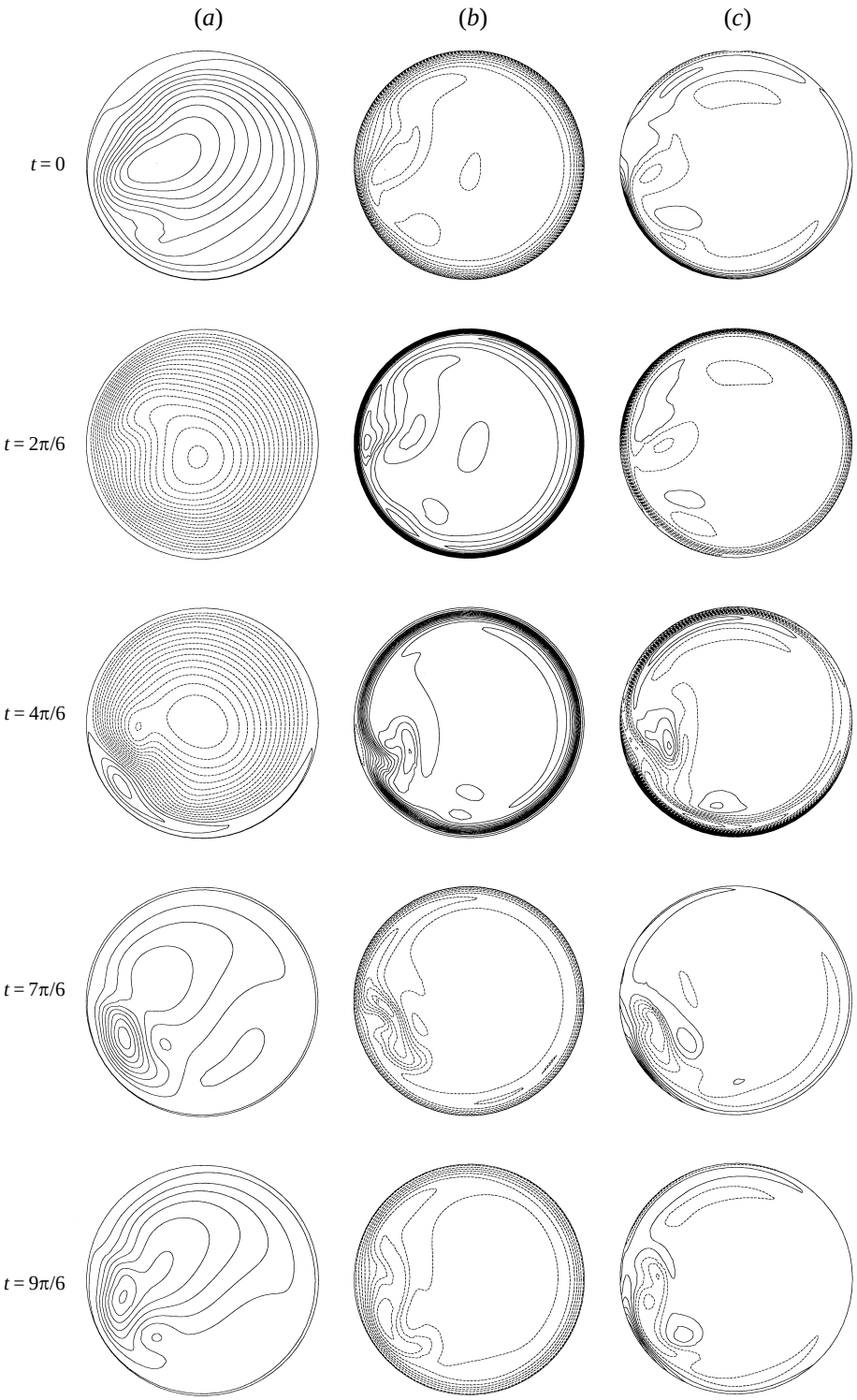

FIGURE 9. Physiological pulsatile flow for $R_s = 80\,h_b, \varepsilon = 1$. (*a*) Ψ, (*b*) v, (*c*) ξ. The separation is less severe than in figure 10. The inside of the bend is on the left.

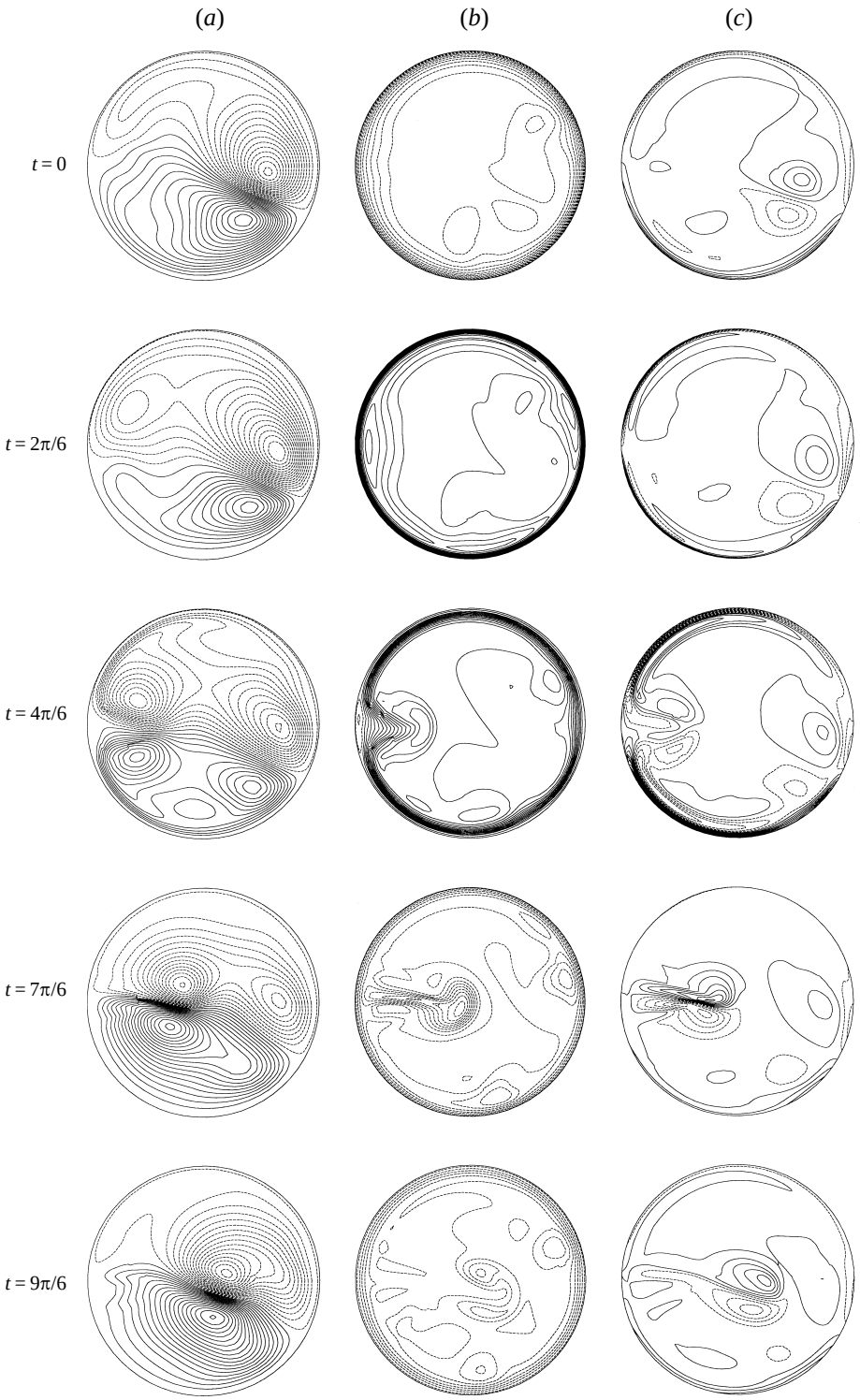

FIGURE 10. Physiological pulsatile flow for $R_s = 80\,h_b, \varepsilon = 10$. (*a*) Ψ, (*b*) v, (*c*) ξ. Separation of a vortex pair near flow reversal which travels across the pipe. The inside of the bend is on the left.

exactly the same region during the flow reversal in late systole ($t = 4\pi/6$) and then slowly evolve near the inner bend throughout the diastolic phase. In general, however, v is quite uniform in the interior with the steep gradient at the boundary resembling the structure for small R_s. The vorticity ξ is accumulated mostly within the layer at the wall and only when the flow reverses is a pair of counter-rotating vortices created by the associated separation. This pair also stays close to the boundary in the region where most of the vorticity is concentrated in the diastolic phase.

In order to discover the effect of torsion the motion described above has to be contrasted with the fluid behaviour in axisymmetry when the pipe has purely planar curvature. Figure 10 portrays the flow at $R_s = 80\,h_b$, $\varepsilon = 10$ which also corresponds to a physiologically relevant regime. Since torsion vanishes in the limit $\varepsilon \to \infty$, the solution must now be almost symmetric in ϕ, and indeed the secondary motion exhibits a two-vortex structure similar to the Dean pattern for a steady pressure gradient. Such an effect has already been observed in the regime $\alpha R_s \ll 1$ when it follows from the small-α asymptotics. Then, the streamfunction Ψ, which describes an unsteady one-vortex type motion for helical flow, tends to zero as $\varepsilon \to \infty$ and only the second-order steady flow, possibly with steady streaming vortices, is retained. Numerical simulations suggest that this mechanism is also valid in the physiologically relevant regime which has important consequences. The two-vortex secondary motion generates much stronger separation during the flow reversal. Now the contours of v are pulled from the wall in a direction normal to the boundary (see figure 10, $t = 7\pi/6$). This creates a pair of counter-rotating ξ vortices with quite strong circulation which during diastole absorb all the vorticity and travel across the pipe cross-section towards the outer bend. Then ξ is transported through the boundary layers at the top and bottom in the systolic phase and the whole cycle repeats. This is associated with the particularly large cross-pipe velocities across the middle of the cross-section where separated shear layers can be observed. In general, flow conditions in the axisymmetric case are much more severe and non-zero torsion smooths out the effects of the flow reversal, inhibiting separation and retaining the vorticity close to the boundary. As a result a simpler structure is formed in the helical case which agrees better with experimental observations. A strong secondary motion across the pipe (figure 10, $t = 7\pi/6$) is uncommon in physiology and high shearing velocities in the middle of the pipe could possibly damage the red cells and proteins in the bloodstream. Hence, one may postulate that the genuinely three-dimensional bends in the body have evolved partly in order to limit it. The trapping of the separated region along the inner bend (figure 9, $t = 7\pi/6$) and the larger variation of the velocity v near the inner wall (figure 9, $t = 4\pi/6, 7\pi/6$ contrasted with figure 10, $t = 7\pi/6$) is physically more appealing, and has indeed been observed experimentally (Chandran 1993).

4.3.1. *Wall shear stress*

The distribution of shear stresses along the boundary is probably the fluid mechanical factor of greatest interest in physiological applications. It is commonly accepted nowadays that the flow patterns and forces acting on the arterial wall play an important and significant role in the initiation and early stages of atherosclerosis, whatever the biochemical genesis may be (Giddens *et al.* 1993). A number of medical and experimental observations indicate there is a strong correlation between shear stress distributions and preferential sites for accumulation of fatty residues. Unfortunately, so far such a mechanism has not been completely understood. The theory proposed by Caro *et al.* (1971) predicts that low-shear regions are more atherogenic. In simple terms, those parts of the boundary where tangential shearing forces are relatively

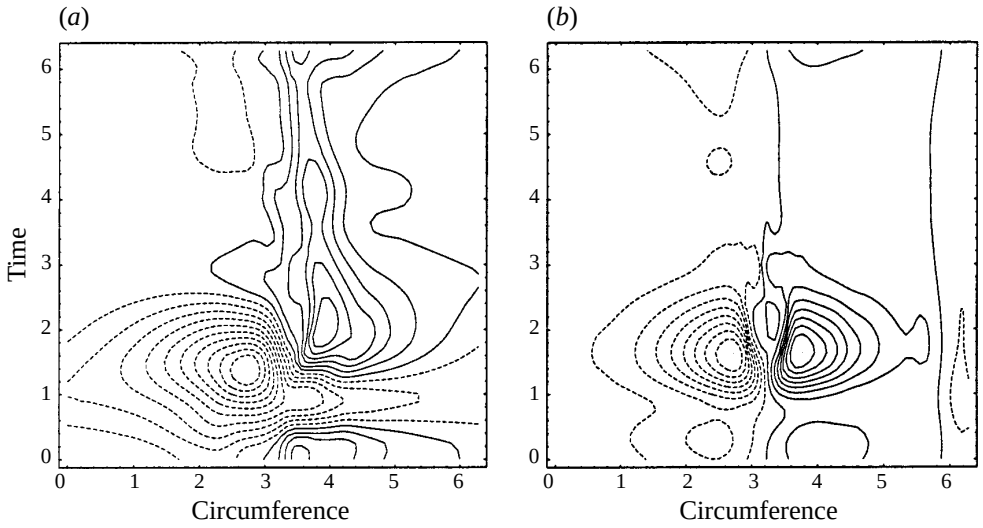

FIGURE 11. Cross-pipe component of wall shear stress for $R_s = 80\,h_b$. (*a*) $\varepsilon = 1$; (*b*) $\varepsilon = 10$. The shear is low at the inside of the bend for the nearly axisymmetric $\varepsilon = 10$, with high spatial shear gradients.

small are deprived of the cleaning effect of the blood flow and are therefore more likely to attract various particles carried by the fluid.

In numerical simulations, for a given computed flow the wall shear stress can be easily obtained and the effect of non-planar helical curvature can be investigated. The down-pipe $\boldsymbol{H}$-component of the shear does not seem to be particularly affected by torsion. Qualitatively a universal spatial distribution is found, with maximum on the inside and minimum on the outside while the time variation essentially follows figure 8. At some points near the inner wall relatively large negative values are reached in late systole. For $\varepsilon = 1$, the spatial profiles exhibit slightly smaller variation than in approximate axisymmetry and in the limit $\varepsilon \to 0$ the distribution becomes completely uniform. The cross-pipe shear is usually expected to be dominated by the down-pipe component, but for non-planar bends in the physiological case it is certainly significant and near the inner bend its magnitude may reach 50% of the down-pipe shear. In figure 11, the distributions in time and space of the cross-pipe wall shear during the cardiac time cycle in the helical ($\varepsilon = 1$) and nearly axisymmetric ($\varepsilon = 10$) cases are shown. The circumference is traversed from the outer point in an anticlockwise direction, so that the intervals $(0, \pi)$, $(\pi, 2\pi)$ correspond respectively to the bottom and top of the pipe. In axisymmetry, the distribution is antisymmetric in ϕ for all time. Then, most of the spatial variation is concentrated in systole while during the diastolic phase the shear is fairly uniform and small. The stress is zero at the point on the inner bend which near the systolic peak is immediately surrounded by the two regions of rather high shear of opposite sign. When torsion is introduced the symmetry is lost and the lower of these regions is pushed into the diastolic phase where it is fairly uniformly smeared out in time. Hence the maximum positive and negative shear now appear at different times, and the stress on the inner wall is no longer zero. This is illustrated by the contours in figure 11 and suggests the general conclusion that torsion decreases instantaneous spatial shear variation during systole while slightly increasing the stress on the inner wall throughout the whole of the diastolic phase. Helical curvature may therefore improve the cleansing of the inner

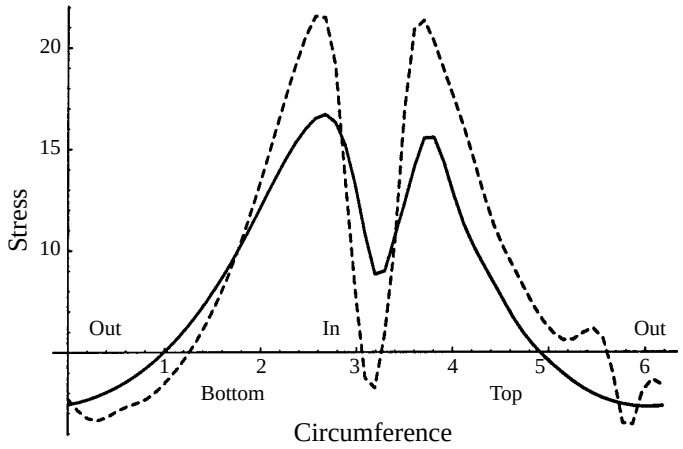

FIGURE 12. R.m.s. time-average of cross-pipe wall shear stress. Solid line $\varepsilon = 1$, dashed line $\varepsilon = 10$. The helical flow has a tendency to reduce stress variation.

bend and, as has been already mentioned, limits the severity of separation during flow reversal. On the other hand, systole occupies only up to 1/3 of the cardiac cycle and it is not obvious what measure of the wall shear, instantaneous behaviour, peak or time-average, controls the distribution of atheroma. The r.m.s. of the shear round the boundary is plotted in figure 12. The variation is less pronounced for the helical bend.

Atherosclerosis usually occurs near arterial bifurcations where closed recirculating zones can be formed downstream in the branches (Naumann & Schmidt-Schonbein 1983). Such separated regions are usually observed in systole and may completely disappear or become fairly uniform during the rest of the time-cycle. Certainly the helical model developed in the present work cannot demonstrate such a phenomenon which would violate the assumed downstream invariance. Yet atherosclerotic lesions often occur in helical patterns, suggesting that the low-shear regions follow approximately helical paths (Fox *et al.* 1982 and Masawa, Glagov & Zarins 1994). The behaviour shown in figure 11, especially during the systolic phase, provides evidence of the equalizing effect of torsion on the wall shear stress distribution. Furthermore, a helical bend upstream of an arterial bifurcation, with its associated uniformly strong cross-pipe flow, could well limit the severity of downstream separation. There seems to be some evidence that more optimal flow patterns may derive from non-planar bends and bifurcations. Helical geometry may play a beneficial rôle in the macro-circulation with some tendency to inhibit the formation of atherosclerotic lesions.

The authors would like to acknowledge with gratitude various helpful discussions with C. G. Caro and J. T. Stuart. Dr Zabielski was supported partly by grants from the Jan Dzienisiewicz Trust, the *Tempus* programme and the Harry Jones fund.

REFERENCES

BERGER, S. A., TALBOT, L. & YAO, L. S. 1983 Flow in curved pipes. *Ann. Rev. Fluid Mech.* **15**, 461–512.

BLENNERHASSETT, P. 1976 Secondary motion and diffusion in unsteady flow in a curved pipe. PhD thesis, Imperial College, London.

CARO C. G., DOORLY, D. J., TARNAWSKI, M., SCOTT, K. T., LONG, Q. & DUMOULIN, C. L. 1996

Non-planar curvature and branching of arteries and non-planar-type of flow. *Proc. R. Soc. Lond.* A **452**, 185–197.

Caro C. G., Fitz-Gerald, J. M. & Schroter, R. C. 1971 Atheroma and arter ial wall shear: Observation, correlation and proposal of a shear dependent mass transfer mechanism of atherogenesis. *Proc. R. Soc. Lond.* B **177**, 109–159.

Chandran K. B. 1993 Flow dynamics in the human aorta. *J. Biomech. Engng* **115**, 611–616.

Childress S., Landman M. & Strauss H. 1989 Steady motion with helical symmetry at large Reynolds number. In *Proc. IUTAM Symp. on Topological Fluid dynamics* (ed. H. K. Moffatt & A. Tsinober), pp. 216–224. Cambridge University Press.

Davies P. F. 1995 Flow-mediated endothelial mechano-transduction. *Physiol. Rev.* **75**, 519–558.

Dean W. R. 1928 The streamline motion of fluid in a curved pipe. *Phil. Mag.* **5**, 673–695.

Dobrin P. B., Litooy F. N., Endean E. D. 1989 Mechanical factors predisposing to intimal hyperplasia and medical thickening in autogenous vein grafts. *Surgery* **105**, 393–400.

Dritschel, D. G. 1991 Generalised helical Beltrami flows in hydrodynamics and magnetohydrodynamics. *J. Fluid Mech.* **222**, 525–541.

Fletcher C. A. J. 1991 *Computational Techniques in Fluid Dynamics.* Springer.

Fox B., James K., Morgan B. & Seed W.A. 1982 Distortion of fatty and fibrous plaques in young human coronary arteries. *Atherosclerosis* **41**, 337–347.

Giddens D. P., Zarins C. K. & Glagov S. 1993 The role of fluid mechanics in the localization and detection of atherosclerosis. *J. Biomech. Engng* **115**, 588–594.

Kamiya A. & Togawa T. 1980 Adaptive regulation of wall shear stress to flow change in the canine artery. *Am. J. Physiol.* **239**, H14–H21.

Landman M. 1990 Time dependent helical waves in rotating pipe flow. *J. Fluid Mech.* **221**, 289–310.

Lynch D. G., Waters S. L. & Pedley T. J. 1996 Flow in a tube with non-uniform, time-dependent curvature: governing equations and simple examples. *J. Fluid Mech.* **323**, 237–265.

Lyne W. H. 1970 Unsteady viscous flow in a curved pipe. *J. Fluid Mech.* **45**, 13–31.

McDonald D. A. 1974 *Blood Flow in Arteries.* Southampton: The Camelot Press Ltd.

Masawa N., Glagov S. & Zarins C. K. 1994 Quantitative morphological study of intimal thickening at the human carotid bifurcation. *Atherosclerosis* **107**, 137–146.

Moore D. R., Weiss N. O. & Wilkins J. M. 1980 The reliability of numerical experiments: transition to chaos in thermosolutant convection. *Nonlinearity* **3**, 997–1014.

Naumann A. & Schmidt-Schonbein H. 1983 A fluid-dynamicist's and a physiologist's look at arterial flow and arteriosclerosis. In *Fluid Dynamics as a Localising Factor for Atherosclerosis* (ed. G. Schettler). Springer.

Pedley T. J. 1980 *The Fluid Mechanics of Large Blood Vessels.* Cambridge University Press.

Pedley T. J. 1995 High Reynolds number flow in tubes of complex geometry with application to wall shear stress in arteries. In *Biological Fluid Dynamics, 49th SEB Symposium.* The Society for Experimental Biology.

Schettler G., Nerem R. M., Schmidt-Schonbein H., Morl H. & Diehm D. (eds.) 1983 *Fluid Dynamics as a Localising Factor for Atherosclerosis.* Springer.

Smith F. T. 1975 Pulsatile flow in curved pipes. *J. Fluid Mech.* **71**, 15–42.

Strikwerda J. C. 1989 *Finite Difference Schemes and Partial Differential Equations.* Wadswirth & Brooks/Cole.

Yoshida Y., Yamaguchi T., Caro C. G., Glagov S. & Nerem R. M. (eds) 1988 *Role of Blood Flow in Artherogenesis.* Springer.

Zabielski, L. 1996 Helical pipe flows in haemodynamics. PhD thesis, Imperial College, London.

Zabielski, L. & Mestel, A. J. 1998 Steady flow in a helically symmetric pipe. *J. Fluid Mech.* **370**, 297–320 (referred to herein as ZM1).